Nanoscale

Accepted Manuscript

This article can be cited before page numbers have been issued, to do this please use: S. Mondal, S. Mitra, F. Fantuzzi and K. Mukherjee, *Nanoscale*, 2026, DOI: 10.1039/D6NR00194G.

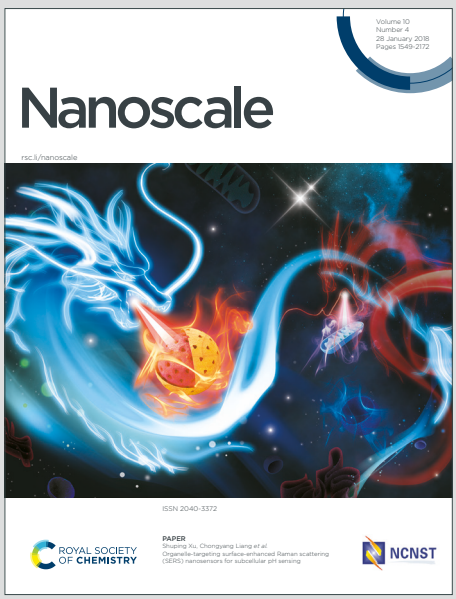

ROYAL SOCIETY OF CHEMISTRY

rsc.li/nanoscale

View Article Online
DOI: 10.1039/D6NR00194G

Synergistic Carbon Black-Supported Nickel-Iron Hydroxide Nanocomposite for Selective Electrochemical Discrimination of Dihydroxybenzene Isomers

Suman Mondal,[1] Shirsendu Mitra,[2]* Felipe Fantuzzi,[3]* Kalisadhan Mukherjee[1]*

[1] Department of Chemistry, Pandit Deendayal Energy University, Gandhinagar, Gujarat-382007, India

[2] Department of Chemical Engineering, Pandit Deendayal Energy University, Gandhinagar, Gujarat-382007, India

[3] Supramolecular, Interfacial and Synthetic Chemistry, School of Natural Sciences, University of Kent, Park Wood Rd, Canterbury CT2 7NH, UK

*S.M. (Email: Shirsendu.Mitra@sot.pdpu.ac.in)

*F.F. (Email: f.fantuzzi@kent.ac.uk)

*K.M. (Email: kalisadhan.mukherjee@sot.pdpu.ac.in)

Abstract

Detection and simultaneous discrimination of dihydroxybenzene (DHB) isomers, particularly catechol (CT) and hydroquinone (HQ), remain challenging due to their closely similar electrochemical responses and partially overlapping redox potentials. These difficulties become more pronounced in binary mixtures, where signal interference complicates analysis across wide concentration ranges. In this work, we report a carbon black-supported nickel-iron hydroxide nanocomposite as a low-cost, non-enzymatic electrochemical sensing material operating at neutral pH, implemented on both conventional electrodes and disposable strip sensors. The optimized sensor showed clear peak separation for CT and HQ, including in equimolar (1:1) mixtures, and achieved limits of detection down to 0.01 micromolar on the glassy carbon platform and 0.05 micromolar on the strip sensor. The sensing platform also showed excellent repeatability over more than 5000 continuous measurements and strong reproducibility over extended time intervals. In addition, statistical descriptors of the voltammetric responses, including skewness and kurtosis, are used as complementary tools to analyze concentration-dependent signal variations. Physicochemical characterization of the nanocomposite supports the proposed interpretation of the observed electrocatalytic performance.

Keywords: Dihydroxybenzene; Metal hydroxide; Electrochemical sensor; Machine learning

View Article Online
DOI: 10.1039/D6NR00194G

1. Introduction

Catechol (CT) and hydroquinone (HQ) are phenolic compounds and structural isomers of dihydroxybenzene (DHB). Although they share the same molecular formula, differences in the relative positions of the hydroxyl groups on the benzene ring result in distinct physicochemical properties, toxicological profiles, and industrial applications. These compounds can be absorbed through the skin and mucous membranes, allowing entry into systemic circulation. Acute exposure may induce toxic effects such as fatigue, headache, dizziness, and pallor, while prolonged or high-level exposure can lead to nephrotoxic and hepatotoxic outcomes, resulting in kidney and liver impairment. Additionally, CT and HQ can disrupt normal nervous system function and cause observable neurotoxic effects.[1, 2] Therefore, their accurate, selective, and simultaneous detection is of significant importance. International organizations, including the World Health Organization (WHO), the European Union (EU), and regulatory agencies in China and the United States have classified them as priority pollutants due to their adverse effects on human health and ecosystems.[3-5] Both compounds are widely used as chemical precursors in the manufacture of plastics, cosmetics, pesticides, and synthetic dyes,[6-8] and contamination of water resources frequently occurs through industrial effluents. These compounds are also considered carcinogenic and may cause damage to the liver and respiratory system in humans.[9, 10] In aquatic environments, CT and HQ are toxic to living organisms, disrupt ecological balance, and can contribute to reduced crop yields in agricultural areas.[11-13] Moreover, they are often found together in environmental matrices, which complicates their selective detection and separation.[14, 15]

Various sophisticated analytical techniques have been reported for the identification of DHB isomers, including spectrophotometry, fluorescence analysis, mass spectrometry..[16-18] In contrast, electrochemical analysis offers a promising alternative due to its low cost, rapid response, simple operation, high sensitivity, and wide linear detection range for monitoring phenolic pollutants.[19-22] Thus, the development of electrochemical sensors is demanding for the reliable individual and simultaneous determination of DHB isomers.

The efficiency of an electrochemical sensor largely relies on the electrocatalytic properties of the electrode materials used.[23-25] In this context, nanostructured transition metal oxides, hydroxides, as well as p-block metal oxides, have gained considerable attention due to their versatile physicochemical properties and wide applications[26-29] Among them, nickel-iron hydroxides have emerged as promising electrocatalytic materials owing to their synergistic

View Article Online
DOI: 10.1039/D6NR00194G

redox activity, tunable surface chemistry, and high environmental stability. The primitive nickel-iron hydroxides when combined with conductive nanocarbons, the resulting nanocomposites exhibit advantageous characteristics, including increased effective surface area, superior electron transfer kinetics.[30]

In this study, a novel carbon black-supported nickel-iron hydroxide (hereafter abbreviated as NFH) nanocomposite was synthesized, systematically characterized, and applied to both conventional three-electrode configurations and screen-printed sensor platforms for the simultaneous determination of catechol and hydroquinone. Electrochemical measurements, including cyclic voltammetry (CV), differential pulse voltammetry (DPV), and square wave voltammetry (SWV), showed strong analytical performance, with detection limits as low as 0.01 μM on traditional electrodes and 0.05 μM on portable, miniaturized platforms. Statistical evaluation of the electrochemical signals using skewness and kurtosis analyses was employed to examine concentration-dependent signal variations. In addition, regression analysis based on datasets obtained from multiple parametric studies highlights the overall sensing characteristics of the proposed platform. These results demonstrate the effectiveness of combining nanocomposite materials with complementary data analysis to achieve selective and sensitive platforms for DHB isomer detection, with strong potential for rapid on-site environmental monitoring.

2. Experimental Section

2.1 Synthesis and Structural Characterizations of NFH

NFH was synthesized using a modified co-precipitation method, as reported in our previous work.[31] Briefly, stoichiometric amounts of nickel(II) nitrate hexahydrate ($Ni(NO_3)_2 \cdot 6H_2O$, (0.017 mol) and ferric(III) nitrate nonahydrate ($Fe(NO_3)_3 \cdot 9H_2O$, (0.034 mol) were dissolved in a minimal volume of ethanol in an Erlenmeyer flask under continuous stirring to ensure complete homogenization. The molar ratio of Ni:Fe in the precursor solution was therefore 1:2. Subsequently, a mixed solution containing triethylamine (TEA, 20 mL) and ethanol (10 mL) was added dropwise (≈1 mL min^{-1}) to the metal salt solution under continuous stirring at room temperature (≈25 °C), leading to the formation of a precipitate. The reaction medium evolved from mildly acidic conditions to a basic environment (final pH ≈ 9–10), promoting the formation of the nickel-iron hydroxide phase. TEA acts not only as a mild base to regulate the pH, but also as a coordinating agent capable of interacting with Ni^{2+} and Fe^{3+} ions, thereby influencing nucleation and growth of the hydroxide network. The resulting material was then

dried at room temperature and used directly for sensing studies. A portion of the dried sample was further calcined at 600 °C for 5 h solely to examine phase evolution, while all electrochemical measurements were performed using the as-prepared hydroxide material. A variety of complementary analytical techniques e.g. FTIR, Raman spectroscopy, XRD, TGA, FE-SEM, and XPS were employed to investigate phase formation, crystalline structure, microstructural features, and elemental composition of the synthesized NFH. The details of instruments for structural characterisations and input parameter for measurement are given in S1.3.

2.3 Electrochemical Measurements

Electrochemical measurements were performed using a standard three-electrode configuration consisting of a glassy carbon electrode (GCE, 3 mm diameter) as the working electrode, an Ag/AgCl reference electrode, and a platinum wire counter electrode. Prior to modification, the GCE surface was mechanically polished using alumina slurries of decreasing particle sizes (1 μm, 0.3 μm, and 0.05 μm), followed by rinsing with EtOH and deionized (DI) water to remove residual impurities and ensure a clean, reproducible surface. To prepare the sensing materials, carbon black (CB) was incorporated at 10, 20, 30, 40, and 50 wt% to obtain a series of CB/NFH nanocomposites. Each composite was dispersed in a 3:2 (v/v) isopropyl alcohol (IPA)/DI water mixture and sonicated for 1 h to achieve uniform dispersion. The resulting ink was drop-cast onto the electrode surfaces using volumes of 9 μL for the GCE and 4 μL for the screen-printed carbon electrode (SPCE), followed by drying under infrared light for 1 h prior to sensing measurements.

All electrochemical experiments were performed in 0.1 M phosphate-buffered saline (PBS, pH 7), prepared using DI water, as described in the Supporting Information (**Figure S1**). The pH was selected based on preliminary optimization studies, which identified pH 7 as providing the highest electrochemical response while also representing environmentally relevant conditions (vide infra). CV, DPV, SWV, and amperometric measurements were carried out at room temperature using a Metrohm Autolab VIONIC electrochemical workstation (Netherlands). In CV measurements, the anodic peak current (I_{pa}) corresponds to oxidation processes, while the cathodic peak current (I_{pc}) corresponds to reduction processes. CV was used to identify the oxidation potentials of the DHB isomers, which were subsequently used in DPV and SWV measurements to monitor current responses and evaluate limits of detection (LODs) for both the GCE and SPCE platforms.

View Article Online
DOI: 10.1039/D6NR00194G

2.4 Implementation of Machine Learning Algorithms

Machine learning (ML) algorithms, including linear regression, nonlinear regression, random forest, polynomial fitting, and support vector regression (SVR) with a radial basis function (RBF) kernel, were employed to model electrochemical signal features such as peak current, peak skewness, and peak kurtosis as functions of analyte concentration. These features were extracted from concentration-dependent electrochemical responses obtained for HQ and CT using both GCE and SPCE electrodes. The data-driven modeling approach provided a complementary means to interpret the electrochemical signal characteristics associated with analyte-electrode interactions and to establish correlations between signal descriptors and analyte concentrations, particularly in cases where simple linear relationships were insufficient.

3. Results and Discussion

3.1. Phase Evolution and Crystallinity of the Nickel-Iron Hydroxide Precursor

The thermal behavior of the synthesized NFH was investigated using TGA, and the results were correlated with powder XRD (PXRD) patterns of NFH and crystalline nickel ferrite (600 °C), to elucidate phase evolution during thermal treatment. The TGA curve shown in **Figure 1a** exhibits multiple weight loss stages up to 700 °C. The initial weight loss observed below 150 °C is attributed to the evaporation of surface adsorbed water and residual ethanol.[32] A significant weight loss between 150 and 250 °C is associated with the decomposition of residual TEA. A further gradual weight reduction up to approximately 400 °C corresponds to the elimination of remaining organic species and the dehydroxylation of intermediate nickel-iron hydroxide phases. Notably, the thermal event around 400 °C is associated with precursor decomposition and the initial stages of structural transformation toward the spinel nickel ferrite phase, rather than definitive crystallization. This interpretation is supported by the PXRD pattern of the NF-400 sample calcined at 400 °C (see **Figure S2**), which shows only weak and broadened diffraction features. In contrast, sharp and well-defined PXRD reflections observed at higher calcination temperature (600 °C) confirm the formation of a well-developed nickel ferrite structure. It should be noted that the calcined $NiFe_2O_4$ phase is discussed only to support structural evolution and was not used for electrochemical sensing measurements.

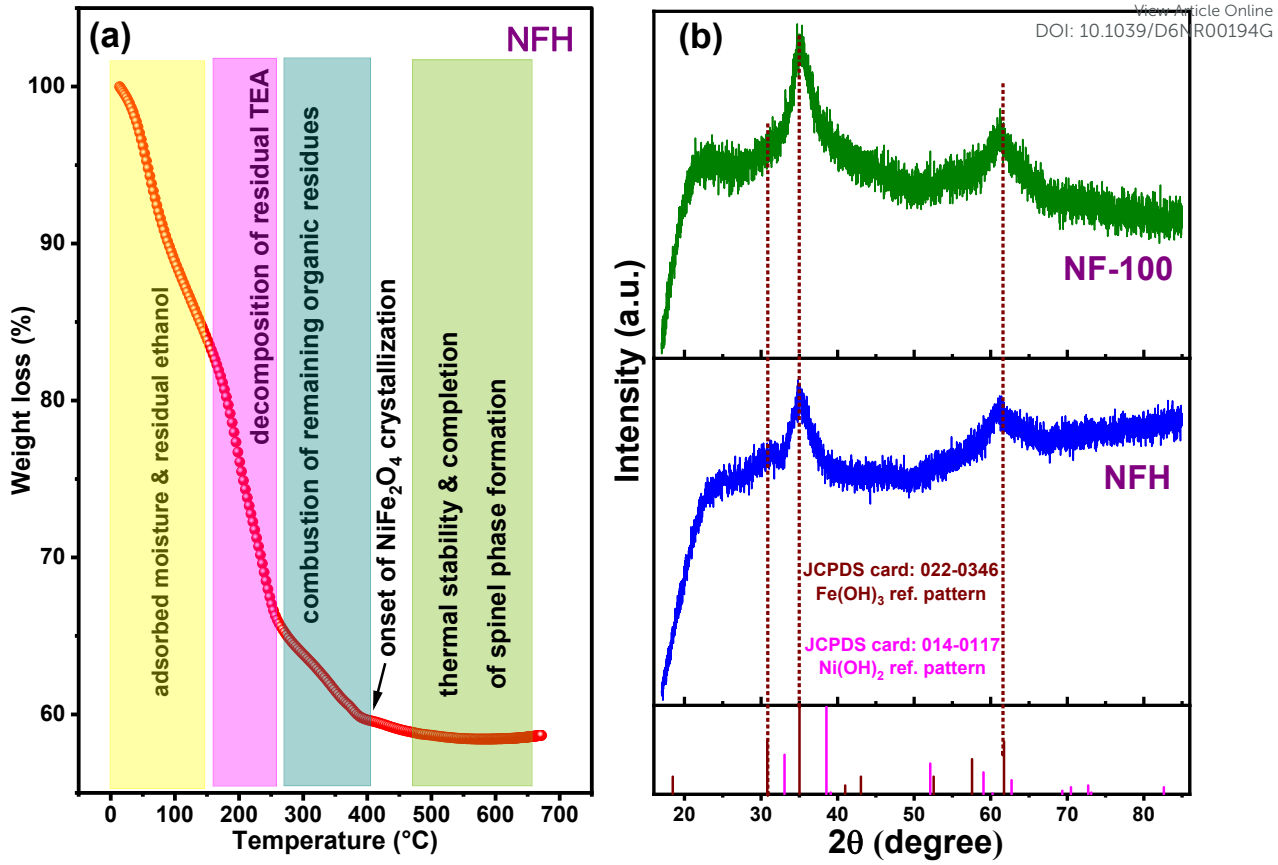

Figure 1. (a) TGA of the NFH xerogel (b) PXRD patterns of the as-prepared NFH hydroxide and the NFH heated at 100 °C (NF-100).

To evaluate the structural phase evolution upon heat treatment, PXRD analysis was performed on the NFH precursor and its thermally treated derivatives. The PXRD patterns presented in **Figure 1b** and Figure S2 reveal a clear temperature-driven transformation of the NFH xerogel into crystalline nickel ferrite. The as-prepared NFH sample exhibits very broad, low intensity diffraction features with maxima centered around approximately $2\theta \approx 34.95°$ and 61.42°. These reflections coincide with the principal diffraction features of $Fe(OH)_3$ (JCPDS 022-0346) and $Ni(OH)_2$ (JCPDS 014-0117), characteristic of a predominantly amorphous nickel-iron mixed hydroxide gel network, rather than a well-defined layered double hydroxide (LDH) or crystalline hydroxide phase formed during the TEA-mediated co-precipitation process.[33] Owing to the highly disordered nature of the material, these broad features are described conservatively as diffuse scattering associated with short-range ordering, rather than being assigned to specific crystalline phases. Upon mild thermal treatment at 100 °C (NF-100), a slight sharpening of the diffuse features is observed, suggesting partial dehydration and local structural rearrangement within the hydroxide framework. The PXRD patterns of both NFH and NF-100 therefore confirm that these materials remain dominated by an amorphous nickel-

iron mixed hydroxide gel network, with only short-range structural correlations consistent with the precursor decomposition regime identified by TGA.

3.2. Vibrational and Chemical Structure Analysis

Raman spectroscopy was employed to probe the structural evolution from the NFH xerogel to the spinel $NiFe_2O_4$ phase. The room-temperature Raman spectrum of the as-synthesized NFH, shown in **Figure 2a**, exhibits broad bands centered at approximately 422 and 533 cm^{-1}, which are attributed to the bending and stretching vibrations of Ni^{II}–O bonds, respectively.[34] In addition, the band observed near 720 cm^{-1} is assigned to Fe^{III}–O or Fe^{III}–O–Ni^{II} vibrational modes characteristic of the mixed-metal hydroxide framework.[34, 35] The absence of distinct low-frequency Raman bands in the 200–400 cm^{-1} region suggests that the formation of a well-ordered LDH structure is unlikely. Instead, the Raman features are more consistent with a mixed nickel-iron hydroxide phase with reduced long-range order. While the presence of highly disordered or turbostratic LDH domains cannot be completely ruled out, the Raman results support the predominance of a non-LDH-type hydroxide structure, which is favorable for electrochemical sensing applications due to its potentially enhanced defect density and accessible active sites.[36] Moreover, the high-frequency band observed near 1048 cm^{-1} is attributed to residual nitrate (NO_3^-) species originating from the nitrate precursors used during synthesis.[37]

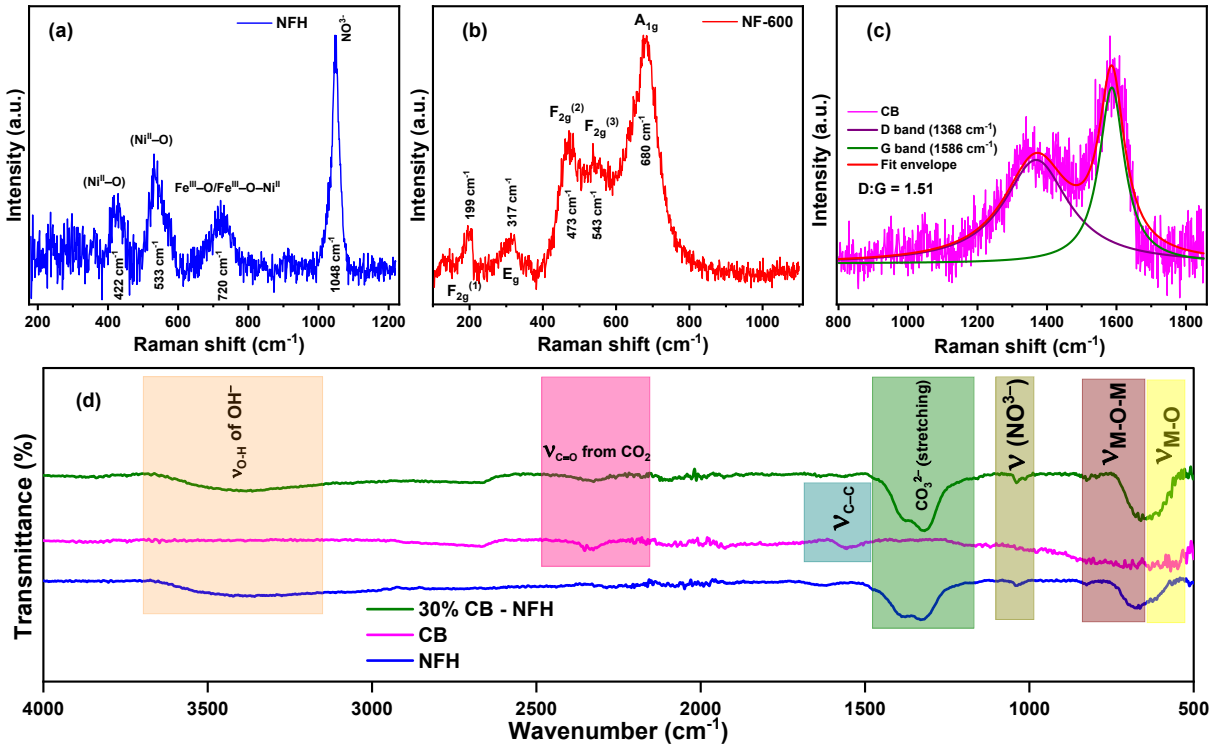

View Article Online
DOI: 10.1039/D6NR00194G

Figure 2. Room-temperature Raman spectra of (a) NFH, (b) NF-600 (c) carbon black, (d) Stacked FTIR spectra of NFH, CB, and the 30% CB/NFH composite.

Upon calcination, the Raman spectrum of the NF-600 sample, shown in **Figure 2b**, displays several well-defined vibrational modes at 199, 317, 473, 543, and 680 cm^{-1}. These peaks are assigned to the $F_{2g}{}^{(1)}$, E_g, $F_{2g}{}^{(2)}$, $F_{2g}{}^{(3)}$, and A_{1g} modes, respectively, which are characteristic of the inverse spinel ferrite structure.[38] The prominent A_{1g} mode at 680 cm^{-1} corresponds to the symmetric stretching vibrations of oxygen atoms coordinated to Fe–O and Ni–O bonds at tetrahedral sites within the spinel $NiFe_2O_4$ lattice. The E_g mode observed at 317 cm^{-1} arises from symmetric bending vibrations of oxygen atoms, while the $F_{2g}{}^{(1)}$ mode is attributed to the translational motion of oxygen ions in tetrahedral units. The $F_{2g}{}^{(2)}$ and $F_{2g}{}^{(3)}$ modes are assigned to asymmetric stretching and bending vibrations of Fe–O and Ni–O bonds, respectively, primarily associated with octahedral sites.[39] The sharpness and clear separation of these Raman bands, together with the disappearance of hydroxide-related vibrational features, are consistent with the transformation of the hydroxide precursor into a well-ordered crystalline spinel $NiFe_2O_4$ phase, in good agreement with the PXRD results.

The Raman spectrum of carbon black (**Figure 2c**) exhibits two prominent features at approximately 1368 cm^{-1} (D band) and 1580 cm^{-1} (G band), corresponding to the disorder-induced A_{1g} breathing mode and the E_{2g} stretching vibration of sp^2-hybridized carbon domains, respectively. The calculated areal intensity ratio of the D and G bands (I_D/I_G) is approximately 1.51, indicating a moderate degree of structural disorder typical of conductive carbon black materials.[40]

The FTIR spectrum of NFH (**Figure 2d**) shows a broad absorption feature in the low-wavenumber region between 600 and 700 cm^{-1}, which can be attributed to combined metal–oxygen (M–O) and metal–oxygen–metal (M–O–M) stretching vibrations within the hydroxide lattice.[41] A broad band centered around 3400 cm^{-1} is assigned to O–H stretching vibrations of hydroxyl groups in the NFH framework. In addition, bands observed at 1388 and 1326 cm^{-1} are attributed to vibrational modes of surface-associated carbonate (CO_3^{2-}) species,[42] likely introduced by atmospheric CO_2 uptake during synthesis and drying. A distinct band near 1560 cm^{-1} is assigned to C–C stretching vibrations of sp^2-hybridized carbon atoms, confirming the graphitic character of the CB surface. In the 30% CB/NFH composite, the O–H stretching band becomes broader and shifts slightly toward lower wavenumbers, suggesting the presence of hydrogen bonding interactions between NFH hydroxyl groups and CB surface functionalities.

View Article Online
DOI: 10.1039/D6NR00194G

Overall, the FTIR and Raman results confirm the successful formation of the composite in which the individual structural characteristics of NFH and CB are preserved. Carbon black not only provides structural support but also introduces surface functionalities that promote stronger interfacial interactions with NFH. These interactions are expected to facilitate charge transport and increase the density of electroactive sites, thereby contributing to the enhanced electrochemical performance observed for the 30% CB/NFH composite.[43]

3.3. Surface Chemistry and Oxidation States

XPS was then employed to examine the surface elemental composition and valence states of the constituent elements in the 30% CB/NFH composite. Binding energies were calibrated against the C 1s peak at 284.8 eV as an internal reference. The survey spectrum of the 30% CB/NFH composite (**Figure 3a**) confirms the presence of Ni, Fe, O, and C elements within the composite structure. High-resolution XPS (HRXPS) spectra of Ni 2p, Fe 2p, O 1s, and C 1s were deconvoluted using a mixed Gaussian–Lorentzian (SGL) line-shape fitting approach with Shirley background correction, implemented using the XPSPEAK41 software.

View Article Online
DOI: 10.1039/D6NR00194G

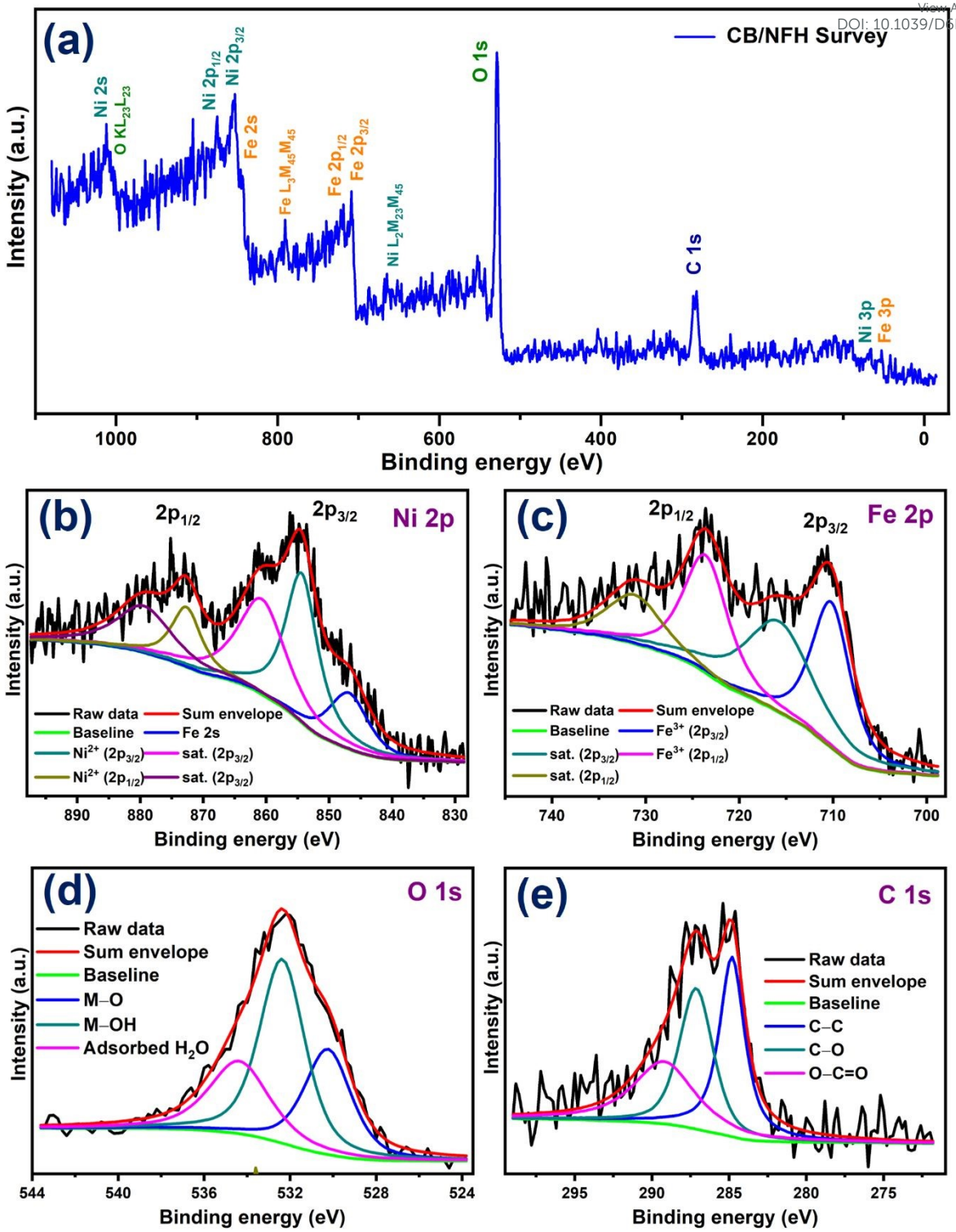

Figure 3. (a) XPS survey spectrum of the 30% CB/NFH composite and peak-fitted high-resolution XPS spectra of (b) Ni 2p, (c) Fe 2p, (d) O 1s, and (e) C 1s

View Article Online
DOI: 10.1039/D6NR00194G

The high-resolution Ni 2p spectrum (**Figure 3b**) is dominated by Ni^{2+} species. The main peaks located at binding energies of approximately 854.36 eV and 872.35 eV are assigned to the Ni $2p_{3/2}$ and Ni $2p_{1/2}$ core levels of Ni^{2+}, respectively. A weak shoulder feature observed at lower binding energy around 846.84 eV is attributed to the Fe 2s orbital. In addition, two satellite peaks appearing at 860.66 and 879.41 eV correspond to characteristic shake-up features associated with the Ni $2p_{3/2}$ and Ni $2p_{1/2}$ orbitals, respectively.[44] While the presence of minor higher-valence Ni species cannot be completely excluded, no distinct spectral features attributable to Ni^{3+} are resolved within the detection limit of the present XPS measurements. The XPS survey spectra yield the following atomic percentages: C 1s (25.22 at. %), O 1s (65.53 at. %), Fe 2p (4.83 at. %), and Ni 2p (4.42 at. %). The surface Ni:Fe ratio is 4.42:4.83 (0.92), indicating a relatively Fe-enriched surface, although closer to equimolar than the nominal precursor composition (Ni:Fe = 1:2).

The HRXPS spectrum of Fe 2p (**Figure 3c**) was deconvoluted into the characteristic spin–orbit split Fe $2p_{3/2}$ and Fe $2p_{1/2}$ components, both corresponding to Fe^{3+} species in the 30% CB/NFH composite. The binding energies of the Fe^{3+} main peaks are observed at 710.19 eV ($2p_{3/2}$) and 723.59 eV ($2p_{1/2}$), while the corresponding satellite peaks appear at 715.72 and 731.18 eV, in good agreement with reported literature values.[45, 46]

The HRXPS spectrum of O 1s (**Figure 3d**) was resolved into three components centered at approximately 530.23, 532.36, and 534.37 eV. The low binding energy peak is assigned to M–O bonds, the dominant intermediate peak corresponds to metal–hydroxyl (M–OH) species, and the high binding energy component is attributed to surface-adsorbed oxygen-containing species such as H_2O or carbonate and residual nitrate species.[46]

The C 1s spectrum (**Figure 3e**) was fitted into three peaks corresponding to C–C (284.79 eV), C–O (287.12 eV) and O–C=O (289.21 eV) functionalities, consistent with the carbon black component within the 30% CB/NFH composite.[47] Overall, the XPS results indicate that the surface composition is dominated by Ni^{2+} and Fe^{3+} species and support the chemical integrity of the CB/NFH composite, while allowing for possible minor higher-valence contributions within the detection limits of XPS.

3.4. Morphology and Elemental Distribution

FESEM micrographs (**Figure 4**) reveal that NFH exhibits a highly porous, agglomerated morphology composed of interconnected nanoparticle clusters. **Figures 4a–c** clearly show a sponge-like surface architecture, suggesting the formation of three-dimensional aggregates

View Article Online
DOI: 10.1039/D6NR00194G

with pronounced surface roughness and a high effective surface area. Such a hierarchical structure is advantageous for electrochemical sensing, as it facilitates efficient electron transfer and enhanced analyte adsorption. Distinct variations in particle packing and porosity across different micrographs can be attributed to localized sample heterogeneities, yet the overall granular texture persists throughout the examined regions.

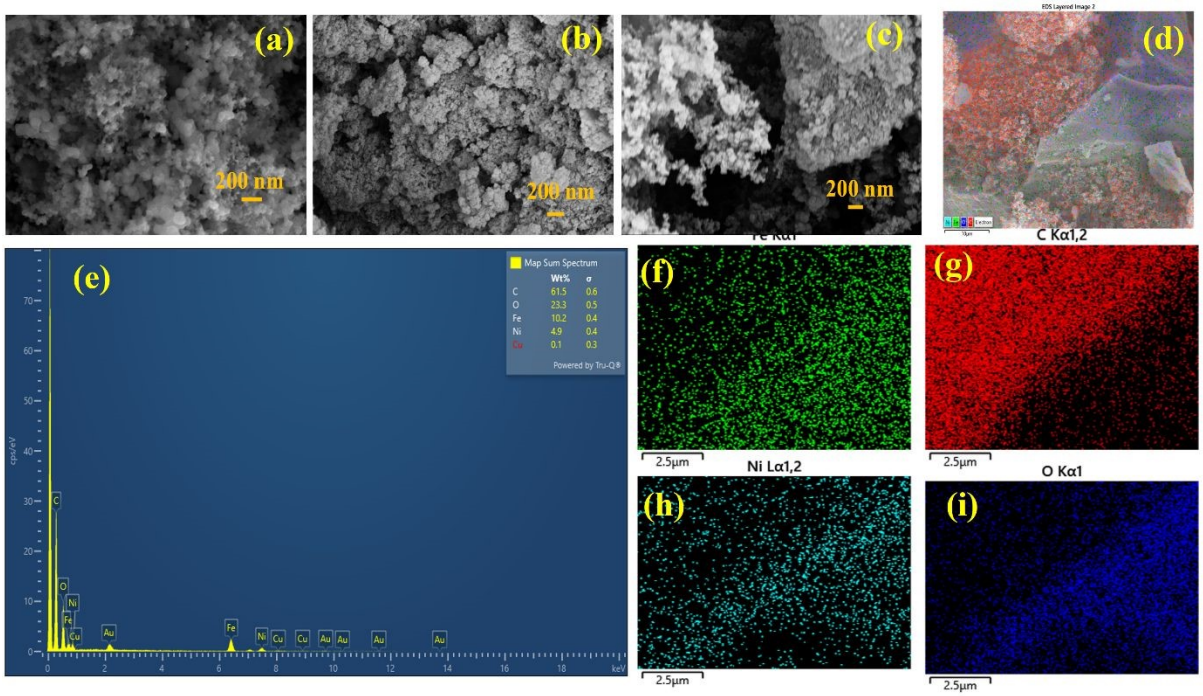

Figure 4. FESEM images of (a) NFH, (b) carbon black, and (c) the 30% CB/NFH composite. (d) EDS elemental mapping and (e) EDS spectrum of the 30% CB/NFH composite, showing the spatial distribution of individual elements: (f) Fe, (g) C, (h) Ni, and (i) O.

Figure 4d presents a composite overlay image for EDS elemental mapping of the sample, highlighting the presence of C, O, Fe, Ni, and trace Cu. The individual elemental map panels (**Figures 4f–i)** demonstrate a homogeneous and uniform distribution of all major elements, with Fe, Ni, and O signals appearing as evenly dispersed features across the imaged area.

In addition to morphological and compositional analysis, the textural properties of the CB/NFH composites were evaluated using nitrogen adsorption–desorption measurements (see **Figure S3**). The 30% CB/NFH sample exhibits the highest specific surface area among the investigated compositions, together with increased pore volume and mesoporous features (~3–4 nm). In contrast, lower CB content results in reduced accessible surface area, while higher CB loading leads to partial pore blocking and aggregation effects. The optimized surface area

View Article Online
DOI: 10.1039/D6NR00194G

and pore structure of the 30% CB composite are therefore consistent with its enhanced electrochemical response.

3.5 Electrochemical Performance of CB/NFH-Modified Electrodes

The CB/NFH/GCE electrode was evaluated for the electrochemical detection of hydroquinone (HQ) and catechol (CT) in a standard three-electrode configuration using 0.1 M PBS at pH 7.0 and a scan rate of 50 mV s^{-1}. Cyclic voltammetry measurements using the bare GCE exhibited negligible current responses within the potential window of –0.4 to 0.6 V versus Ag/AgCl, indicating minimal electrochemical activity toward HQ and CT oxidation. In contrast, the CB/NFH-modified GCE displayed well-defined oxidation peaks at approximately 0.09 V for HQ and 0.19 V for CT. The appearance of these peaks indicates that the CB/NFH nanocomposite effectively promotes the electrocatalytic oxidation of both analytes, resulting in enhanced sensitivity and selectivity compared to the unmodified electrode.

3.5.1 Optimization and Fundamental Electrochemical Behavior

To identify the most efficient composite composition, all prepared CB/NFH nanocomposites were tested for the electrochemical detection of 50 μM catechol, as shown in **Figure 5a**. The comparison revealed that the electrode containing 30% CB exhibited the highest peak current among all tested compositions (**Figure 5b**), indicating superior electrocatalytic activity under these conditions. This behavior can be rationalized by considering the balance between conductivity and active-site accessibility within the composite. At lower CB contents, the conductive network is not sufficiently developed, leading to reduced electron transfer efficiency. In contrast, higher CB loadings may promote partial aggregation and limit exposure of catalytically active NFH sites, as well as reduce effective mass transport. The 30% CB composition therefore provides an optimal balance between electrical conductivity and accessible active surface area, consistent with both the electrochemical response and textural analysis. Consequently, CV measurements were carried out using the 30% CB/NFH/GCE electrode at scan rates ranging from 10 to 130 mV s^{-1} in a 0.1 M PBS buffer solution containing both HQ and CT. As the scan rate increased, the oxidation and reduction peak currents of HQ and CT increased proportionally, accompanied by slight shifts in peak potentials (**Figure 5c**). This suggests efficient and stable electron transfer at the electrode surface.

View Article Online
DOI: 10.1039/D6NR00194G

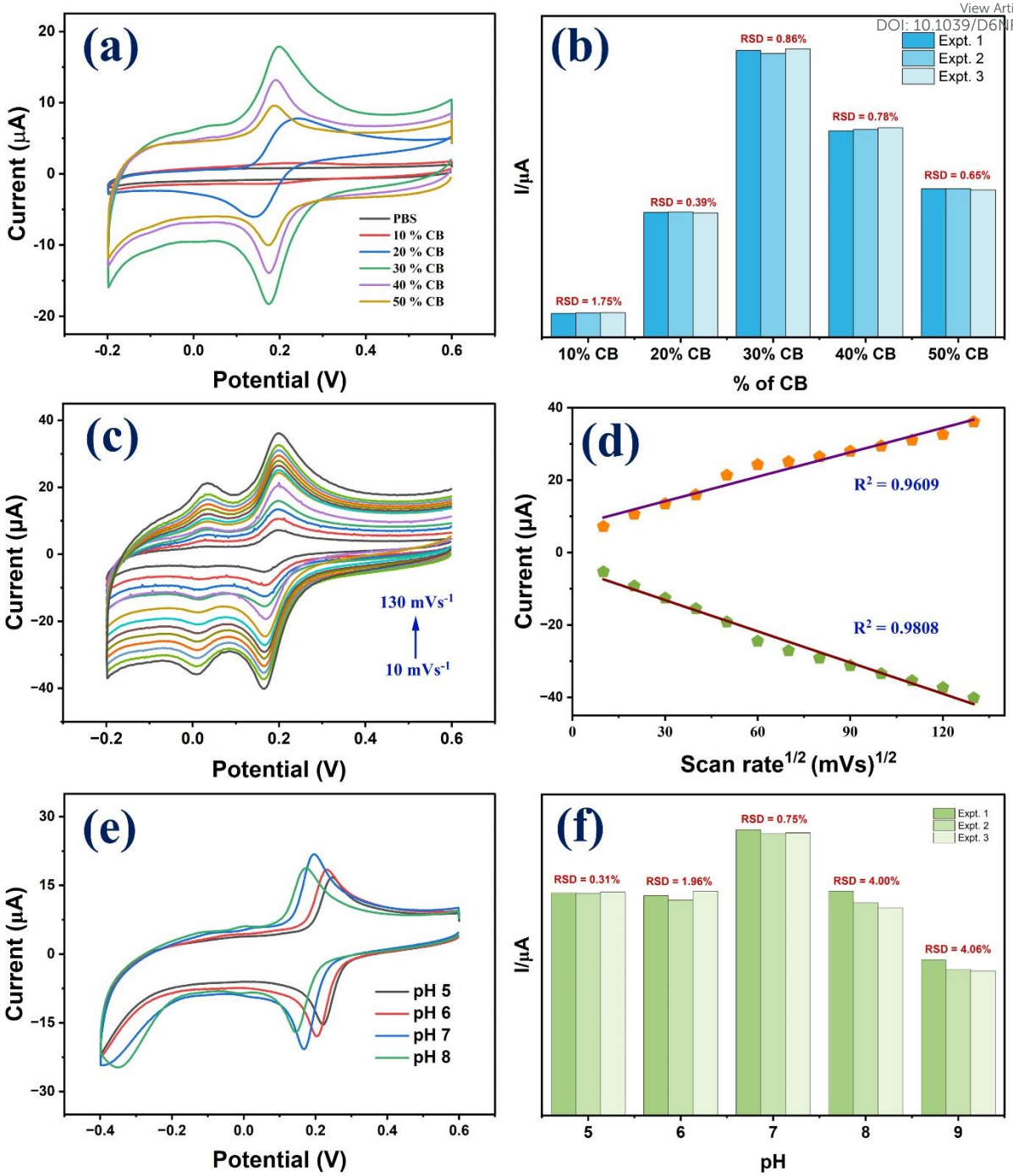

Figure 5. (a) Cyclic voltammograms (CVs) and (b) corresponding peak current values obtained using CB/NFH-based electrodes for the detection of 50 μM catechol. (c) CVs recorded at different scan rates for HQ and CT mixtures using the 30% CB/NFH composite. (d) Linear relationship between peak current and the square root of scan rate. (e) CVs recorded at different pH values and (f) corresponding bar plot of peak current responses.

View Article Online
DOI: 10.1039/D6NR00194G

A clear linear relationship between the peak current and the square root of the scan rate was observed (**Figure 5d**), suggesting that the redox reactions of HQ and CT are predominantly controlled by diffusion of electroactive species from the bulk solution to the electrode surface. Using the Randles–Ševčík equation for a diffusion-controlled process, the diffusion coefficient was estimated to be on the order of 10^{-6} cm^2 s^{-1} (see Supporting Information for details), assuming a two-electron oxidation process consistent with phenolic compounds. Moreover, the small potential separation between anodic and cathodic peaks is consistent with a quasi-reversible redox process. The high regression coefficients ($R^2 \approx 0.96–0.98$) further demonstrate the good electrochemical performance and reliability of the 30% CB/NFH/GCE electrode for HQ and CT detection.[48, 49]

To further distinguish the kinetic regime, a log–log plot of peak current (Ip) versus scan rate (v) was constructed as shown in **Figure S4**. The obtained linear relationship exhibited a slope of 0.63, which is close to the theoretical value of 0.5 expected for a diffusion-controlled process. This result indicates that the process is predominantly diffusion-controlled, with possible minor contributions from surface effects.

Additionally, the electrochemically active surface area (ECSA) was estimated from the double-layer capacitance (Cdl) obtained by cyclic voltammetry in the non-Faradaic region. The Cdl values were 9.09, 1.36, and 8.47 mF cm^{-2} for CB, NFH, and CB–NFH (30% CB), respectively (**Figure S5**). Both CB and CB–NFH exhibited significantly higher ECSA than NFH, with the composite showing a surface area comparable to CB. The incorporation of NFH mainly provides additional catalytic sites that enhance electron-transfer kinetics and peak separation, rather than significantly increasing the surface area.

The CV response of the 30% CB/NFH/GCE electrode toward 50 μM HQ and CT was examined over a pH range of 5.0–8.0 at a scan rate of 50 mV s^{-1} (**Figure 5e**). As the pH increased from 5.0 to 7.0, the oxidation and reduction peak potentials for both analytes shifted toward more negative values, confirming proton involvement in the redox reactions and consistent with Nernstian behavior typical of phenolic compounds.[50] HQ and CT undergo a two-electron, two-proton ($2e^-/2H^+$) oxidation process, consistent with prior reports.[51, 52] The anodic peak currents increased progressively with pH, reaching a maximum at pH 7.0, and then decreased at pH 8.0 (**Figure 5f**), indicating optimal electrocatalytic activity under near-neutral conditions. The corresponding measurements show good repeatability, with relative standard deviation (RSD)

View Article Online
DOI: 10.1039/D6NR00194G

values below 5% for both CB-content optimization and pH studies. At pH 7.0, reduced protonation of electrode surface sites and DHB isomers enhances analyte adsorption and electron transfer kinetics.[53-55] At higher pH values, deprotonation of phenolic hydroxyl groups leads to the formation of negatively charged phenolate ions, while the electrode surface also becomes increasingly negatively charged. The E□ values were calculated using $E_p = \frac{E_1 + E_2}{2}$ and plotted against pH (**Figure S6**). A linear relationship with a slope of approximately −26 mV pH^{-1} was obtained, which is close to the theoretical value of 29.5 mV pH^{-1} (59/2 mV) at 25 °C. This suggests the involvement of two electrons and one proton in the rate-determining step, indicating a proton-coupled electron transfer process with non-ideal proton participation. This may induce electrostatic repulsion, which can limit analyte adsorption and contribute to a decrease in peak currents. Additionally, elevated OH^- concentrations can destabilize the analytes, further suppressing their oxidation responses.[53, 56]

3.5.2 Individual Detection of Catechol and Hydroquinone

Figure 6a presents the CV plots recorded at the 30% CB/NFH-modified GCE in the presence of CT concentrations ranging from 10 to 400 μM. The corresponding anodic and cathodic peak currents extracted from Figure 6a exhibit a linear dependence on CT concentration, as illustrated in **Figure 6b**. Similar variations in peak currents are observed during the detection of HQ (**Figure 6c**), and the corresponding linear relationship between peak current and HQ concentration is shown in **Figure 6d**. In both cases, the redox peak currents increase proportionally with analyte concentration, with good linearity and high correlation coefficients (R^2), demonstrating the reliable quantitative response of the 30% CB/NFH-modified electrode toward both DHB isomers.

View Article Online
DOI: 10.1039/D6NR00194G

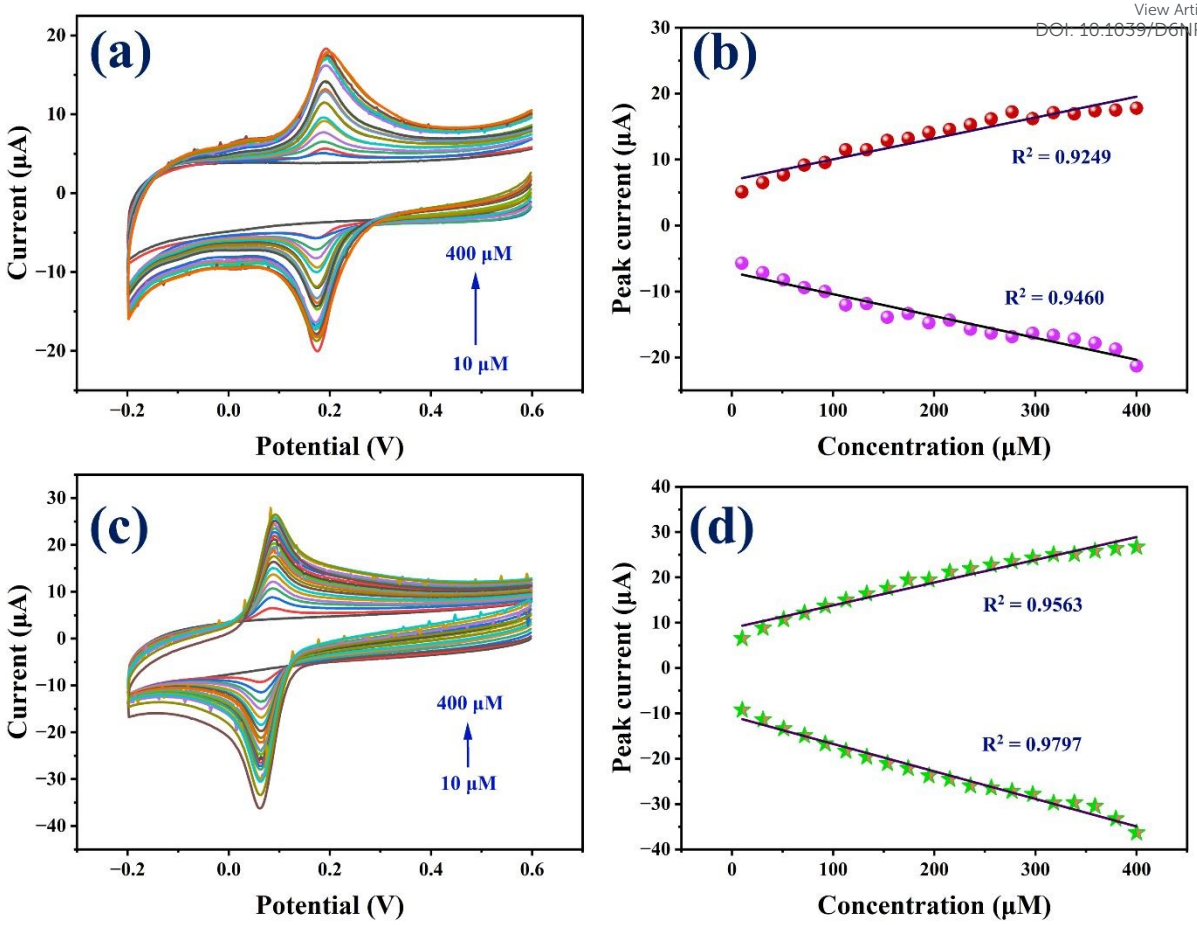

Figure 6. (a) CVs recorded at the 30% CB/NFH-modified GCE for catechol (CT) at different concentrations. (b) Corresponding calibration plot showing the variation of anodic and cathodic peak currents with CT concentration. (c) CVs illustrating the concentration-dependent response of hydroquinone (HQ). (d) Corresponding calibration plot showing the variation of anodic and cathodic peak currents with HQ concentration.

3.5.3 Simultaneous Detection of DHB Isomers on GCE and SPCE

A range of electrochemical techniques, including CV, differential pulse voltammetry (DPV), and square wave voltammetry (SWV), was systematically employed to assess the sensing performance of 30% CB/NFH-modified GCE and SPCE toward DHB isomers. Among them, DPV was primarily used for quantitative detection owing to its higher sensitivity and superior peak resolution compared to CV.

The DPV responses for CT detection using the CB/NFH-modified GCE are shown in **Figures S7a–b**, with the concentration of HQ maintained at a constant value. In these measurements, the CT concentration was varied from 0.03 μM to 200 μM. Similarly,

View Article Online
DOI: 10.1039/D6NR00194G

Figures S7c–d present the DPV responses for HQ detection using the same electrode while keeping the CT concentration constant. In all cases, the anodic peak current increased progressively with increasing analyte concentration, consistent with diffusion-controlled electrochemical behavior and effective electrocatalytic activity of the 30% CB/NFH composite. The presence of well-defined and clearly separated oxidation peaks for CT and HQ demonstrates the ability of the modified electrodes to reliably distinguish between the two isomers, even in mixed solutions.

In addition to DPV and SWV, CV was employed to examine the redox characteristics and concentration-dependent current responses of CT and HQ using the 30% CB/NFH-modified SPCE. The corresponding CV curves are presented in **Figures S8a** and **S8c**. A near-linear increase in peak current with increasing analyte concentration was observed. However, owing to inherent limitations of SPCEs, including higher background noise and lower current sensitivity compared to GCEs, DPV signals became less stable at very low analyte concentrations. Consequently, SWV was employed for low-concentration measurements, providing improved signal resolution and lower detection limits, as shown in **Figures S8b** and **S8d**. The SWV responses exhibit well-defined current peaks at low micromolar to sub micromolar concentrations, highlighting the high sensitivity of the 30% CB/NFH/SPCE sensor.

Analysis of the complete electrochemical dataset reveals that the oxidation peak currents of both CT and HQ increase proportionally with analyte concentration. For the 30% CB/NFH/GCE, a linear response range of 0.03 μM to 200 μM was obtained, whereas the 30% CB/NFH/SPCE exhibited a linear working range between 0.15 μM and 200 μM. The limit of detections (LoDs) for CT and HQ over the 30% CB/NFH/GCE and 30% CB/NFH/SPCE are estimated to be 0.01 μM and 0.05 μM considering the LoD is 3 times lower than limit of quantification. The slightly higher detection limit observed for the SPCE can be attributed to its smaller electroactive surface area relative to the GCE. Nonetheless, both electrode platforms demonstrate good stability, reproducibility, and selectivity toward individual DHB isomers. These results indicate that the 30% CB/NFH-modified electrodes effectively combine high electrocatalytic activity with strong signal reproducibility, enabling sensitive and simultaneous determination of catechol and hydroquinone in complex matrices.

In practical environmental scenarios, catechol and hydroquinone often coexist in water samples, making it essential to evaluate the ability of the sensing platform to distinguish between these isomers under competitive conditions. To this end, interference studies were

View Article Online
DOI: 10.1039/D6NR00194G

conducted by monitoring the electrochemical response of one analyte while maintaining the concentration of the other at a fixed level. The results further support the selectivity and simultaneous detection capability of the 30% CB/NFH-modified electrodes toward DHB isomers.

Under optimized experimental conditions, the 30% CB/NFH-modified GCE was evaluated using both CV and DPV. For CV measurements, a potential window from −0.2 V to 0.6 V was applied, while for DPV analysis the range was slightly narrowed to −0.1 V to 0.5 V to improve signal resolution. As shown in **Figures 7a** and **7b**, the anodic peak current corresponding to HQ oxidation increased proportionally with increasing concentration, exhibiting a wide linear range from 0.1 µM to 400 µM. The presence of well-defined and clearly separated oxidation peaks indicates that the 30% CB/NFH/GCE electrode can sensitively detect HQ even in the presence of CT, demonstrating strong anti-interference capability.

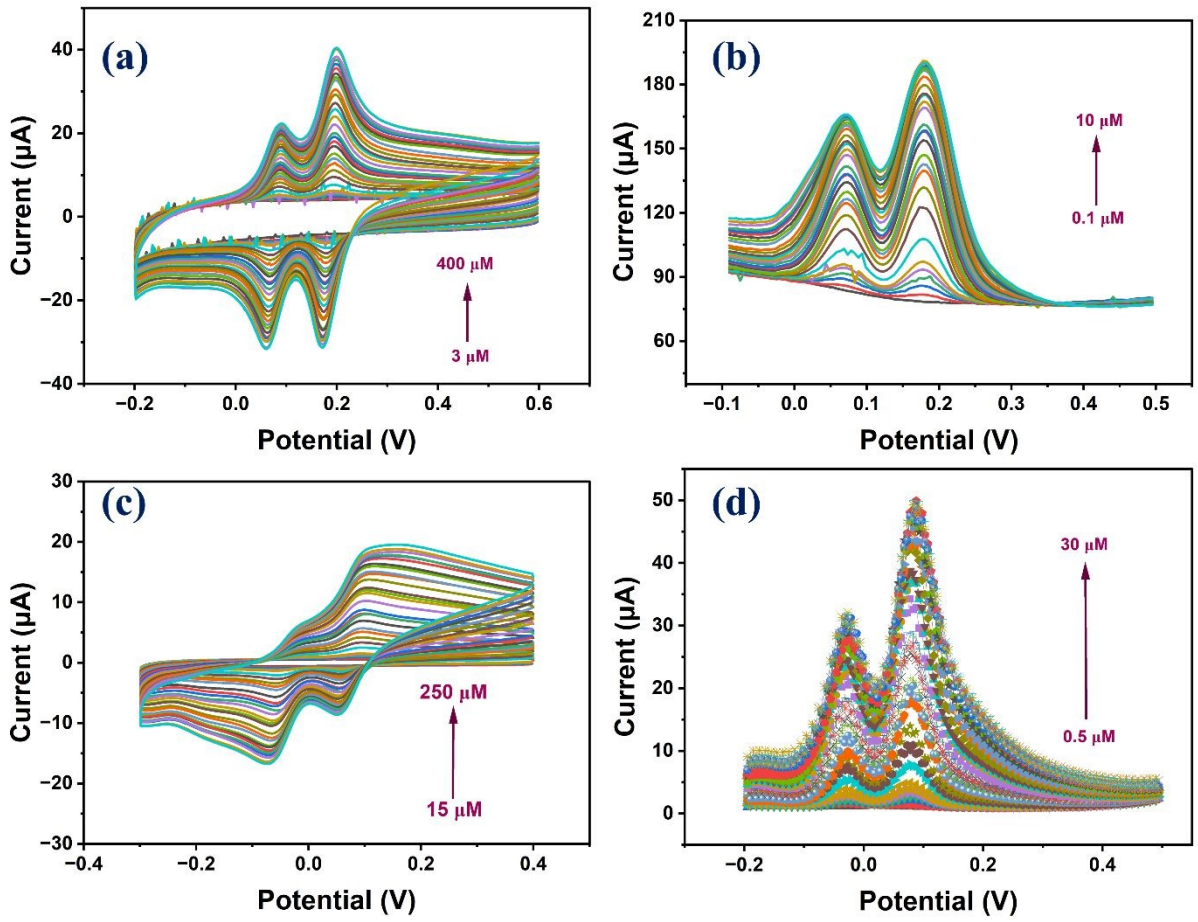

View Article Online
DOI: 10.1039/D6NR00194G

Figure 7. (a) CV (b) DPV responses for detection of different concentrations DHB isomer mixtures over 30% CB/NFH-modified GCE (c) CV (d) SWV responses for detection of different concentrations DHB mixture over 30% CB/NFH/SPCE.

Similarly, the 30% CB/NFH-modified SPCE electrode was employed for the analysis of binary CT and HQ mixtures using both CV and SWV, as shown in **Figures 7c** and **7d**. For CV measurements, the applied potential window ranged from −0.25 V to 0.4 V, while for SWV a window of −0.2 V to 0.5 V was selected to ensure clear separation of the oxidation peaks corresponding to the two isomers. The SPCE platform enabled efficient detection of CT and HQ in mixed solutions over a linear range of 0.5 μM to 250 μM. The gradual and proportional increase in oxidation peak currents with analyte concentration indicates stable and reproducible electrocatalytic activity of the 30% CB/NFH composite on SPCE surfaces.

Overall, these results demonstrate that both 30% CB/NFH/GCE and 30% CB/NFH/SPCE electrodes exhibit high selectivity and sensitivity for the simultaneous determination of CT and HQ. A comparison with recently reported DHB isomer sensors is provided in Table S2 (Supporting Information), confirming that the present platform offers competitive detection limits together with the advantage of a portable SPCE configuration. [6, 57-62] The clear peak separation and broad linear detection ranges highlight the strong potential of these modified electrodes for practical applications in monitoring DHB isomers in environmental and wastewater samples.

3.5.4 Reproducibility, Stability, Spike Recovery, and Selectivity of the 30% CB/NFH-Modified GCE

Figure 8a shows the DPV responses of the 30% CB/NFH-modified GCE toward HQ (50 μM) and CT (50 μM) recorded over 25 consecutive measurements. **Figure 8b** illustrates the long-term electrochemical stability of the electrode, evaluated by CV over 5000 continuous cycles in the presence of 250 μM of DHB isomer mixtures. In both cases, the DPV and CV profiles remained largely unchanged, with no significant variation in the oxidation peak currents of HQ and CT, indicating efficient short-term reproducibility and long-term electrochemical stability.

View Article Online
DOI: 10.1039/D6NR00194G

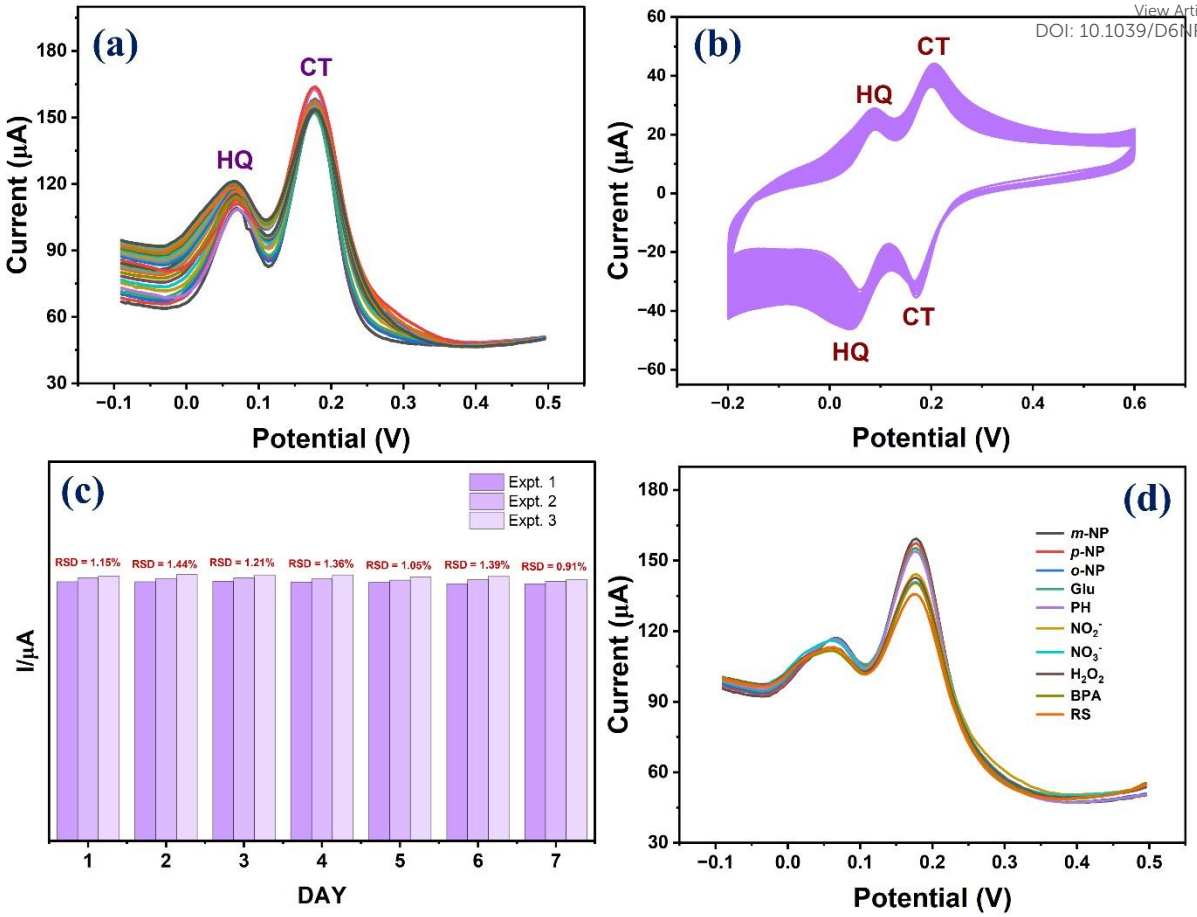

Figure 8. (a) DPV response of 30% CB/NFH-modified GCE towards 50 μM HQ and CT (50 μM) over 25 consecutive measurements. (b) CV response of 30% CB/NFH-modified GCE towards 250 μM HQ and CT over 5000 consecutive cycles. (c) Repeatability and long-term stability evaluation of the 30% CB/NFH/GCE for detection of 50 μM CT over a period of 1–7 days. (d) DPV responses of the 30% CB/NFH/GCE towards 50 μM HQ and CT in presence of a five-fold excess of potential interfering species, including *m*-NP, *p*-NP, *o*-NP, Glu, PH, NO_2^-, NO_3^-, H_2O_2, BPA, and RS, recorded in 0.1 M PBS solution (pH 7.0).

To further assess operational durability, DPV measurements were performed for CT (50 μM) over several consecutive days. The day-wise DPV responses, presented in **Figure 8c**, clearly illustrate the consistent peak current intensities and stable peak potentials throughout the testing period, indicating excellent temporal stability and robustness of the 30% CB/NFH/GCE for detection of DHB isomers.

The selectivity of the sensor was evaluated by introducing common potential interferents into PBS containing HQ and CT. As shown in **Figure 8d**, DPV responses were recorded in the presence of a five-fold excess of various interferent species, including *meta*-nitrophenol (*m*-

View Article Online
DOI: 10.1039/D6NR00194G

NP), *para*-nitrophenol (*p*-NP), *ortho*-nitrophenol (*o*-NP), glucose (Glu), phenol (PH), nitrite (NO_2^-), nitrate (NO_3^-), hydrogen peroxide (H_2O_2), bisphenol A (BPA), and resorcinol (RS). The oxidation peak currents corresponding to HQ (50 μM) and CT (50 μM) remained unaltered upon the addition of these interferents, indicating good selectivity and anti-interference capability of 30% CB/NFH/GCE during simultaneous electrochemical detection.

The selective sensing of HQ and CT can be attributed primarily to two key factors. First, the carbon black component of the nanocomposite consists of highly carbonized domains rich in aromatic rings, which may promote preferential adsorption of HQ and CT through π–π interactions. Second, the oxidation potentials of HQ and CT, typically occurring between 0 and +0.4 V, are significantly lower than those of the tested interfering phenolic and redox-active species, resulting in well-separated and interference-free oxidation peaks.[63] Overall, these results indicate that the 30% CB/NFH nanocomposite provides a stable, selective, and reliable electrochemical platform for the simultaneous sensing of DHB isomers.

To evaluate the practical applicability of the developed sensor, spike–recovery experiments were carried out using real water samples. The collected samples were filtered and spiked with known concentrations of the target analyte within the linear detection range (10–45 μM). The electrochemical measurements were performed under identical experimental conditions, and the concentrations were calculated using the calibration equation obtained from the CV analysis. The calculated recovery values ranged from approximately 75% to 118% (see Supporting Table S3), reflecting matrix effects and possible interferences present in real samples. Despite this variability, the results suggest that the sensor is capable of detecting the analyte in complex environmental matrices, highlighting its potential applicability for environmental monitoring.

3.6 Peak-Shape Analysis and Machine-Learning-Assisted Modeling

The previous section demonstrated that DPV enables the detection of HQ and CT at significantly lower concentrations than CV. This observation is consistent with prior reports,[64] which have shown that DPV offers enhanced sensitivity and improved peak resolution compared to CV. Furthermore, DPV is particularly effective at resolving overlapping signals arising from multicomponent systems. Owing to these advantages, DPV signals were further analyzed to extract additional concentration-dependent features.

DPV measurements were recorded over a wide range of analyte concentrations, and the resulting peaks were analyzed in terms of peak current (**Figure 9a**), peak skewness (**Figure**

View Article Online
DOI: 10.1039/D6NR00194G

9b), and peak kurtosis (**Figure 9c**). While peak current directly correlates with analyte concentration and forms the basis of calibration, peak skewness and kurtosis provide additional information related to electrode–analyte interactions and signal characteristics. These peak characteristics are influenced by redox kinetics, diffusion and convection processes, and surface adsorption phenomena occurring at the electrode–electrolyte interface.

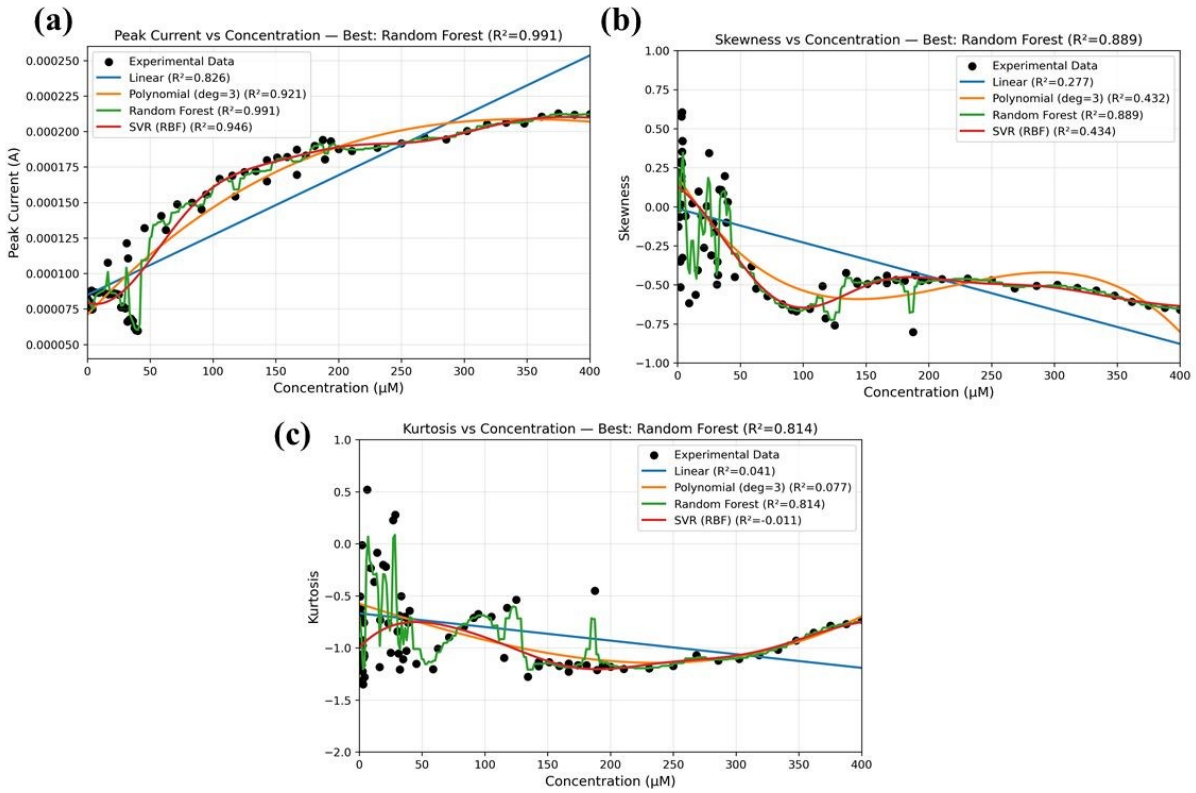

Figure 9. Scatter plots (black circles) showing the variation of (a) peak current, (b) peak skewness, and (c) peak kurtosis as a function of hydroquinone concentration. The experimental data are fitted using different machine-learning models, including linear regression, polynomial regression, random forest, and support vector regression (SVR) with a radial basis function (RBF) kernel.

As shown in **Figure 9a**, the DPV peak currents for HQ exhibit noticeable fluctuations at concentrations below 50 μM. Such variations can be attributed to factors including low signal intensity, background noise, and non-uniform adsorption of the analyte on the electrode surface at low surface coverage. As the concentration increases beyond 50 μM, the peak current initially rises in a nonlinear manner before approaching a saturation regime. This nonlinear increase may reflect contributions from both diffusion and surface-related processes, where interfacial effects become more pronounced. At higher concentrations (above 200 μM), the

View Article Online
DOI: 10.1039/D6NR00194G

current response reaches a quasi-saturation region, which may arise from surface site saturation, mass-transport limitations, or partial electrode fouling.

Overall, this progression reflects a transition from noise-dominated behavior at low concentrations, to kinetically influenced response at intermediate concentrations, and finally to diffusion-limited behavior at high concentrations. These results suggest that the fabricated electrode provides reliable quantitative estimation of HQ at concentrations above 50 μM, while earlier results indicate that qualitative detection remains feasible in the submicromolar concentration range.

For quantitative evaluation of electrode performance, analysis of peak skewness is used to describe the symmetry of DPV peak shapes. Peak skewness reflects asymmetry in the electrochemical response: positive values correspond to right-tailed peaks, typically associated with slower diffusion or electron-transfer processes, whereas negative values indicate left-tailed peaks, which may arise from adsorption effects or overlapping electrochemical processes. Similar to the behavior observed for peak current, the skewness values of the DPV peaks for HQ exhibit pronounced fluctuations at concentrations below 50 μM, reflecting poorly defined peak symmetry caused by low signal intensity and increased surface noise. As the concentration increases beyond 50 μM, the skewness values progressively stabilize within the range of −0.5 to −0.6, indicating the emergence of a consistent left-tailed asymmetry in the peak profile. The stabilization of negative skewness is consistent with increased contributions from adsorption or preconcentration processes at higher analyte concentrations, resulting in more uniform electrochemical responses.

On the other hand, kurtosis in DPV signals describes the sharpness of the peak profile, where higher values are generally associated with narrower and more defined redox responses, while lower values correspond to broader peaks that may arise from diffusion-limited or mixed electrochemical processes. Consistent with the trends observed for peak current and peak skewness, the kurtosis values of the hydroquinone DPV peaks exhibit pronounced fluctuations at concentrations below 50 μM, reflecting poorly defined peak shapes due to low analyte response and increased background noise. With increasing concentration, the kurtosis values gradually increase from approximately −1.2 to −0.65, indicating a progressive narrowing and stabilization of the peak profiles. This transition from strongly negative to moderately negative kurtosis is consistent with improved signal definition as the signal-to-noise ratio increases.

Overall, the observed kurtosis trends indicate improved consistency of the electrode response under conditions of sufficiently high signal-to-noise ratio.

In contrast to HQ, the peak current response for CT does not exhibit significant fluctuations even at concentrations as low as 10 μM, indicating a more stable electrochemical response across the investigated concentration range (**Figure 10a**). The skewness values display noticeable variability at concentrations below 25 μM, followed by convergence toward a relatively constant negative value as the concentration increases (**Figure 10b**). Beyond 25 μM, the stabilized negative skewness corresponds to the formation of a reproducible left-tailed peak profile, consistent with adsorption-influenced or preconcentration effects becoming more dominant at higher analyte levels. This transition from fluctuating to stable skewness reflects improved signal definition and a more consistent electrochemical response once sufficient analyte coverage is achieved at the electrode surface.

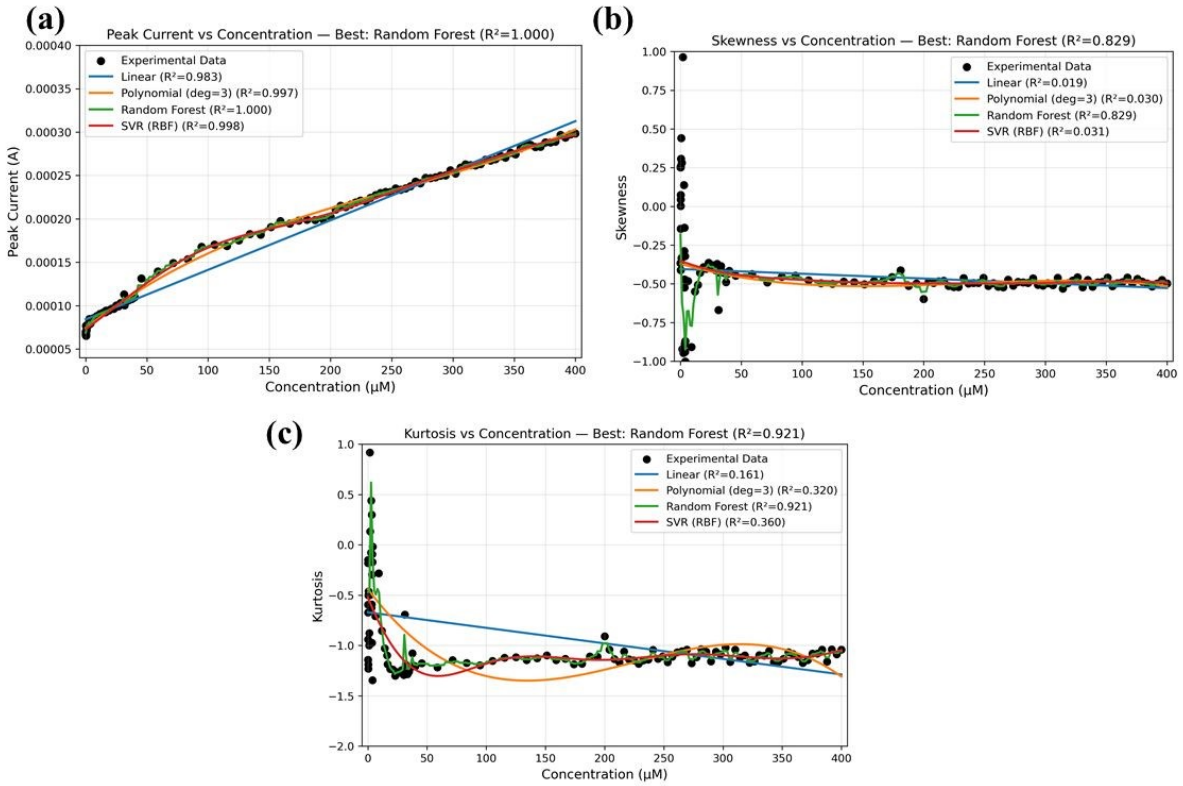

Figure 10. Scatter plots (black circles) showing the variation of (a) peak current, (b) peak skewness, and (c) peak kurtosis as a function of catechol concentration. The experimental data are fitted using different machine-learning models, including linear regression, polynomial regression, random forest, and support vector regression (SVR) with a radial basis function (RBF) kernel.

View Article Online
DOI: 10.1039/D6NR00194G

A similar trend is observed for kurtosis. At concentrations below 25 μM, kurtosis values fluctuate substantially, indicating poorly defined peak shapes associated with low signal-to-noise ratio and weak faradaic response. As the concentration increases beyond 25 μM, the kurtosis values stabilize around approximately −1.2 (**Figure 10c**), corresponding to consistently broader and flatter peak profiles relative to a Gaussian distribution. Such platykurtic behavior is commonly associated with diffusion-influenced or overlapping electrochemical processes and indicates a steady, reproducible peak shape at higher analyte concentrations. Overall, the stabilization of both skewness and kurtosis above 25 μM reflects improved signal consistency and reproducible electrochemical behavior for catechol detection.

Consistent with the HQ analysis, the CT peak descriptors were further modeled using multiple machine-learning algorithms. Owing to the reduced signal fluctuations relative to HQ, improved R^2 coefficients were obtained, particularly for polynomial regression and random forest models. These fitted relationships may serve as useful calibration functions for quantification of CT.

To characterize the electrochemical response of the SPCE electrode, SWV data obtained under experimental conditions were analyzed in detail. Multiple SWV scans were recorded over a range of analyte concentrations for both CT and HQ, and all resolved peaks were systematically evaluated to extract characteristic parameters. For CT, peak current (**Figure S9a**) exhibited a linear dependence on concentration, enabling quantitative calibration. Peak skewness (**Figure S9b**) was analyzed to describe peak asymmetry associated with surface interactions and heterogeneous electron-transfer processes, while peak kurtosis (**Figure S9c**) was used to assess deviations from an ideal Gaussian peak shape arising from electrode–analyte interactions.

Similarly, for HQ, peak current (**Figure S10a**) showed a proportional response to concentration, supporting quantitative determination. Peak skewness (**Figure S10b**) reflected changes in peak asymmetry that may be associated with adsorption or electrostatic interactions at the electrode surface, while peak kurtosis (**Figure S10c**) indicated variations in peak width related to mass-transport effects. Although peak current primarily reflects concentration-dependent faradaic processes, analysis of skewness and kurtosis provides additional descriptors related to electron-transfer kinetics, diffusion, and convection effects, allowing a more complete assessment of SPCE response characteristics toward phenolic analytes.

3.7 Proposed Sensing Mechanism

View Article Online
DOI: 10.1039/D6NR00194G

Based on the combined electrochemical and structural analyses, a plausible sensing mechanism can be proposed. The carbon black component acts as a conductive network that facilitates efficient electron transfer, while the Ni-Fe hydroxide phase provides catalytically active sites for the oxidation of CT and HQ. The oxidation process is predominantly diffusion-controlled, as supported by scan-rate analysis and diffusion coefficient estimation. Adsorption of the aromatic analytes onto the carbon surface via π–π interactions may contribute to enhanced sensitivity. The presence of two well-separated oxidation peaks is consistent with differences in the redox potentials of the isomers, enabling their simultaneous discrimination.

4. Conclusions

The present work reports the development of a carbon black-supported nickel-iron hydroxide nanocomposite as an effective sensing material for the electrochemical detection and discrimination of dihydroxybenzene (DHB) isomers, specifically catechol (CT) and hydroquinone (HQ). Comprehensive physicochemical characterization using XRD, TGA, FTIR, Raman spectroscopy, XPS, and FESEM supports the formation of a nanocomposite structure with favorable electroactive features. Electrochemical evaluations employing CV, DPV, and SWV, conducted on conventional glassy carbon electrodes (GCE) and screen-printed carbon electrodes (SPCE), show high sensitivity and selectivity toward both analytes, including in binary mixtures. The sensing platform achieved limits of detection of 0.01 micromolar for CT and HQ using GCE, and 0.05 micromolar when implemented on SPCE, indicating suitability for trace-level analysis. In addition, the incorporation of machine-learning-based data analysis provided complementary tools for signal interpretation and discrimination between isomeric species, supporting quantitative performance. Overall, the results indicate that the proposed multi-technique sensing platform enables rapid, reproducible, and sensitive analysis of DHB isomers. The demonstrated performance across both laboratory-scale and portable sensing formats suggests potential applicability for environmental monitoring applications, where reliable detection of structurally similar organic pollutants is required.

Acknowledgements

We acknowledge support from the Department of Science and Technology, Government of India (grant CRG/2022/003215). We also thank the Department of Chemistry, Pandit Deendayal Energy University, for institutional support. F.F. acknowledges the Royal Society

ISPF International Collaboration Awards 2024 (Brazil and South Africa) under Grant No. [ICAO\R1\241112] for the NUBIAN project. Technical and professional assistance from Mr. Ayan Roy, Mr. Sourav Ghosh, and Mr. Tarak Nath Das is gratefully acknowledged.

Supporting Information

Additional experimental details include descriptions of materials and methods used in the study, such as preparation of phosphate buffer solution (PBS) with controlled pH and composition. Electrochemical measurements using CV, DPV, and SWV are described in detail. ML-based analysis of the SPCE data is also presented. Further characterization of the synthesized materials using complementary techniques is included to support the main findings. Additional results on sensor selectivity toward potential interfering species, as well as stability and repeatability evaluated through repeated measurements, are provided. Calibration plots used to determine sensor sensitivity and linear response ranges are also included.

Author Information

Corresponding Authors

Kalisadhan Mukherjee - Department of Chemistry, Pandit Deendayal Energy University, Gandhinagar, Gujarat-382426, India; orcid.org/0000-0002-5431-4246.

Email: kalisadhan.mukherjee@sot.pdpu.ac.in

Felipe Fantuzzi – Supramolecular, Interfacial and Synthetic Chemistry, School of Natural Sciences, University of Kent, Park Wood Rd, Canterbury CT2 7NH, UK; orcid.org/0000-0002-8200-8262.

Email: f.fantuzzi@kent.ac.uk

Shirsendu Mitra - Department of Chemical Engineering, Pandit Deendayal Energy University, Gandhinagar, Gujarat-382426, India; orcid.org/0000-0001-9111-7703.

Email: Shirsendu.Mitra@sot.pdpu.ac.in

Authors

Suman Mondal - Department of Chemistry, Pandit Deendayal Energy University, Gandhinagar, Gujarat-382426, India; orcid.org/0009-0000-1355-9434.

Notes

The authors declare no competing financial interest.

View Article Online
DOI: 10.1039/D6NR00194G

References

1. Alu'datt, M. H.; Rababah, T.; Alhamad, M. N.; Al-Mahasneh, M. A.; Almajwal, A.; Gammoh, S.; Ereifej, K.; Johargy, A.; Alli, I., A review of phenolic compounds in oil-bearing plants: Distribution, identification and occurrence of phenolic compounds. *Food Chem.* **2017,** *218*, 99-106.
2. Wang, X.; Wu, M.; Li, H.; Wang, Q.; He, P.; Fang, Y., Simultaneous electrochemical determination of hydroquinone and catechol based on three-dimensional graphene/MWCNTs/BMIMPF6 nanocomposite modified electrode. *Sens. Actuators B Chem.* **2014,** *192*, 452-458.
3. Veerakumar, P.; Sangili, A.; Chen, S.-M.; Kumar, R. S.; Arivalagan, G.; Firdhouse, M. J.; Hameed, K. S.; Sivakumar, S., Photocatalytic degradation of phenolic pollutants over palladium-tungsten trioxide nanocomposite. *Chem. Eng. J.* **2024,** *489*, 151127.
4. Chen, Y.; Liu, X.; Zhang, S.; Yang, L.; Liu, M.; Zhang, Y.; Yao, S., Ultrasensitive and simultaneous detection of hydroquinone, catechol and resorcinol based on the electrochemical co-reduction prepared Au-Pd nanoflower/reduced graphene oxide nanocomposite. *Electrochim. Acta* **2017,** *231*, 677-685.
5. Velmurugan, M.; Karikalan, N.; Chen, S.-M.; Cheng, Y.-H.; Karuppiah, C., Electrochemical preparation of activated graphene oxide for the simultaneous determination of hydroquinone and catechol. *J. Colloid Interface Sci.* **2017,** *500*, 54-62.
6. Huang, W.; Zhang, Z.; Li, Q.; Wang, D.; Xiong, S.; Jiang, X.; Zhou, Y.; Zhao, Q., Metal–Organic Framework-Based Dual-Mode Electrochemical Sensor for Simultaneous Electrochemical Determination of Hydroquinone and Catechol. *Inorganic Chemistry* **2025,** *64* (32), 16564-16571.
7. Fan, J.; Li, J.; Liu, C.; Lu, M.; Jia, X.; Zhao, W.; Yu, A.; Zhang, S., Michael and Schiff-Base Reactions-Assisted Fluorescence Sensor Based on the MOF Nanosheet Microspheres for the Effective Discrimination and Detection of Hydroquinone and Catechol. *Anal. Chem.* **2025,** *97* (3), 1925-1932.
8. Veerakumar, P.; Sangili, A.; Chen, S.-M.; Vinothkumar, V.; Kim, T. H., Octahedral Pt–Ni Alloy Nanoparticles Decorated on 3D Interconnected Porous Carbon Nanosheets for Voltammetric Determination of Dihydroxybenzene Isomers. *ACS Appl. Nano Mater.* **2023,** *6* (21), 19981-19996.
9. Galati, G.; O'brien, P. J., Potential toxicity of flavonoids and other dietary phenolics: significance for their chemopreventive and anticancer properties. *Free Radical Biol. Med.* **2004,** *37* (3), 287-303.
10. Rahman, M. M.; Rahaman, M. S.; Islam, M. R.; Rahman, F.; Mithi, F. M.; Alqahtani, T.; Almikhlafi, M. A.; Alghamdi, S. Q.; Alruwaili, A. S.; Hossain, M. S., Role of phenolic compounds in human disease: current knowledge and future prospects. *Molecules* **2021,** *27* (1), 233.
11. Yu, H.; Liu, S.; Fan, J.; Zhu, S.; Zhao, X.-E.; Liu, Q., Tb-based Metal–Organic Framework-Referenced Fluorescence Assay for Distinguishing Hydroquinone from Its Isomers and Subsequent Quantitative Visual Detection of Cu2+. *Anal. Chem.* **2025,** *97* (3), 1799-1808.
12. Hapani, U.; Highland, H.; George, L.-B., Phenolic compounds: a significant threat to agricultural soils. In *Bioremediation of Emerging Contaminants from Soils*, Elsevier: 2024; pp 97-106.

13. Angon, P. B.; Mondal, S.; Jahan, I.; Datto, M.; Antu, U. B.; Ayshi, F. J.; Islam, M. S., Integrated pest management (IPM) in agriculture and its role in maintaining ecological balance and biodiversity. *Advances in Agriculture* **2023,** *2023* (1), 5546373.
14. Kumar, M.; Swamy, B. K.; Hu, B.; Wang, M.; Yasin, G.; Liang, B.; Madhuchandra, H.; Zhao, W., Electrochemical activation of copper oxide decorated graphene oxide modified carbon paste electrode surface for the simultaneous determination of hazardous Di-hydroxybenzene isomers. *Microchem. J.* **2021,** *168*, 106503.
15. Yin, D.; Liu, J.; Bo, X.; Guo, L., Cobalt-iron selenides embedded in porous carbon nanofibers for simultaneous electrochemical detection of trace of hydroquinone, catechol and resorcinol. *Anal. Chim. Acta* **2020,** *1093*, 35-42.
16. Atta, N. F.; Galal, A.; El-Gohary, A. R., New insight for simultaneous determination of hazardous di-hydroxybenzene isomers at crown ether modified polymer/carbon nanotubes composite sensor. *J. Hazard. Mater.* **2020,** *388*, 122038.
17. Deng, M.; Lin, S.; Bo, X.; Guo, L., Simultaneous and sensitive electrochemical detection of dihydroxybenzene isomers with UiO-66 metal-organic framework/mesoporous carbon. *Talanta* **2017,** *174*, 527-538.
18. Dong, J.; Wen, L.; Liu, H.; Yang, H.; Zhao, J.; Luo, X.; Hou, C.; Huo, D., Simultaneous detection of dihydroxybenzene isomers in the environment by a free-standing flexible ZnCo2O4 nanoplate arrays/carbon fiber cloth electrode. *Sci. Total Environ.* **2023,** *855*, 158878.
19. Ahmad, R.; Khan, M.; Tripathy, N.; Khan, M. I. R.; Khosla, A., Hydrothermally synthesized nickel oxide nanosheets for non-enzymatic electrochemical glucose detection. *J. Electrochem. Soc.* **2020,** *167* (10), 107504.
20. Tigari, G.; Manjunatha, J., A surfactant enhanced novel pencil graphite and carbon nanotube composite paste material as an effective electrochemical sensor for determination of riboflavin. *Journal of Science: Advanced Materials and Devices* **2020,** *5* (1), 56-64.
21. Huo, M.; Sun, H.; Jin, Z.; Liu, W.; Liang, Y.; Liu, J.; Liu, C.; Xing, Z.; Yang, Y.; Chang, J., Tailoring octahedron-tetrahedron synergism in spinel catalysts for acidic water electrolysis. *Journal of the American Chemical Society* **2025,** *147* (12), 10678-10689.
22. Mukherjee, K.; Mondal, S.; Paine, S., Electrochemical Sensors for Quality Control in the Food and Beverage Industry: Materials Science. *Innovation of Chemistry & Materials for Sustainability* **2025,** *2* (2), 107-121.
23. Joseph, X. B.; Baby, J. N.; Wang, S.-F.; Sriram, B.; George, M., Interfacial superassembly of Mo2C@ NiMn-LDH frameworks for electrochemical monitoring of carbendazim fungicide. *ACS Sustain. Chem. Eng.* **2021,** *9* (44), 14900-14910.
24. Sriram, B.; Baby, J. N.; Hsu, Y.-F.; Wang, S.-F.; Benadict Joseph, X.; George, M.; Veerakumar, P.; Lin, K. C., MnCo2O4 microflowers anchored on P-doped g-C3N4 nanosheets as an electrocatalyst for voltammetric determination of the antibiotic drug sulfadiazine. *ACS Applied Electronic Materials* **2021,** *3* (9), 3915-3926.
25. Sriram, B.; Baby, J. N.; Wang, S.-F.; Hsu, Y.-F.; Sherlin V, A.; George, M., Well-designed construction of yttrium orthovanadate confined on graphitic carbon nitride sheets: electrochemical investigation of dimetridazole. *Inorg. Chem.* **2021,** *60* (17), 13150-13160.
26. Kasi, G.; Viswanathan, K.; Sadeghi, K.; Seo, J., Optical, thermal, and structural properties of polyurethane in Mg-doped zinc oxide nanoparticles for antibacterial activity. *Prog. Org. Coat.* **2019,** *133*, 309-315.
27. Karthika, V.; Kaleeswarran, P.; Gopinath, K.; Arumugam, A.; Govindarajan, M.; Alharbi, N. S.; Khaled, J. M.; Al-Anbr, M. N.; Benelli, G., Biocompatible properties of nano-

drug carriers using TiO2-Au embedded on multiwall carbon nanotubes for targeted drug delivery. *Materials Science and Engineering: C* **2018,** *90*, 589-601.

28. Manikandan, P. N.; Dharuman, V., Electrochemical simultaneous sensing of melatonin, dopamine and acetaminophen at platinum doped and decorated alpha iron oxide. *Electroanalysis* **2017,** *29* (6), 1524-1531.

29. Thirumalairajan, S.; Mastelaro, V. R., A novel organic pollutants gas sensing material p-type CuAlO2 microsphere constituted of nanoparticles for environmental remediation. *Sens. Actuators B Chem.* **2016,** *223*, 138-148.

30. Yang, D.; Li, X.; Li, Y.; Song, W.; Yan, T.; Cui, Y.; Yan, L., Capacitive deionization of high concentrations of hexavalent chromium using nickel–ferric-layered double hydroxide/molybdenum disulfide asymmetric electrode. *J. Colloid Interface Sci.* **2023,** *634*, 793-803.

31. Mondal, S.; Roy, A.; Pfeifer, R.; Fantuzzi, F.; Choudhury, A.; Mukherjee, K., Pristine Nanostructured α-Ni (OH) 2 as a Nonenzymatic Electrochemical Strip Sensor for Trace Detection of Phenolic Compounds. *ACS Appl. Nano Mater.* **2025**.

32. Choi, K.-S.; Yeon, J.-W.; Park, Y.-S.; Ha, Y.-K.; Han, S.-H.; Song, K., Investigation of nickel ferrite formation in a binary Fe (III)–Ni (II) hydroxide precipitate containing H2O with or without Li2O doping. *J. Alloys Compd.* **2009,** *486* (1-2), 824-829.

33. Nguyen, A. T. N.; Kim, M.; Shim, J. H., Controlled synthesis of trimetallic nitrogen-incorporated CoNiFe layered double hydroxide electrocatalysts for boosting the oxygen evolution reaction. *RSC Adv.* **2022,** *12* (20), 12891-12901.

34. Zhao, R.; Xu, S.; Liu, D.; Wei, L.; Yang, S.; Yan, X.; Chen, Y.; Zhou, Z.; Su, J.; Guo, L., Modulating the electronic structure of NiFe hydroxide by Zr doping enables industrial-grade current densities for water oxidation. *Applied Catalysis B: Environmental* **2023,** *338*, 123027.

35. Zaffora, A.; Megna, B.; Seminara, B.; Di Franco, F.; Santamaria, M., Ni, Fe, Co-LDH Coated Porous Transport Layers for Zero-Gap Alkaline Water Electrolyzers. *Nanomaterials* **2024,** *14* (5), 407.

36. Jena, M.; Mallick, S.; Rath, A.; Dalai, M. K.; Das, D. P., GQD@ NiFe-LDH Nanosheets for Photocatalytic Activity towards Textile Dye Degradation via Lattice Contraction. *ChemPlusChem* **2023,** *88* (9), e202300276.

37. Zeng, X.; Cai, Z.; Zhang, C.; Wang, D.; Xu, J.; Wang, X., Novel NiFe-LDH@ Ni-MOF/NF heterostructured electrocatalysts for efficient oxygen evolution. *Materials Research Letters* **2022,** *10* (2), 88-96.

38. Kumar, S.; Kumari, K.; Kumar, A.; Koo, B.; Vij, A., Raman spectroscopy of spinel ferrites. In *Ferrite Nanostructured Magnetic Materials*, Elsevier: 2023; pp 537-555.

39. Tiwari, R.; De, M.; Tewari, H.; Ghoshal, S., Structural and magnetic properties of tailored NiFe2O4 nanostructures synthesized using auto-combustion method. *Results in Physics* **2020,** *16*, 102916.

40. Ferrari, A. C.; Robertson, J., Interpretation of Raman spectra of disordered and amorphous carbon. *Physical review B* **2000,** *61* (20), 14095.

41. Shahid, N. F.; Jamal, A.; Haq, G.-u.; Javed, M.; Saifullah, M.; Anjum, M. A. R., Cobalt–iron layered double hydroxide nanosheet-wrapped nitrogen-doped graphite felt as an oxygen-evolving electrode. *Energy Advances* **2023,** *2* (12), 2109-2118.

42. Costa, F. R.; Saphiannikova, M.; Wagenknecht, U.; Heinrich, G., Layered double hydroxide based polymer nanocomposites. In *Wax Crystal Control· Nanocomposites· Stimuli-Responsive Polymers*, Springer: 2007; pp 101-168.

43. Saleh, T. S.; Badawi, A. K.; Salama, R. S.; Mostafa, M. M. M., Design and development of novel composites containing nickel ferrites supported on activated carbon derived from agricultural wastes and its application in water remediation. *Materials* **2023,** *16* (6), 2170.
44. Krishnamurthy, P.; Maiyalagan, T.; Panomsuwan, G.; Jiang, Z.; Rahaman, M., Iron-doped nickel hydroxide nanosheets as efficient electrocatalysts in electrochemical water splitting. *Catalysts* **2023,** *13* (7), 1095.
45. Chen, H.; Fan, Y.; Fan, Z.; Xu, H.; Cui, D.; Xue, C.; Zhang, W., Noble-metal-free pn heterojunction of iron (III) hydroxide and graphitic carbon nitride for hydrogen evolution reaction. *Ceram. Int.* **2021,** *47* (24), 35057-35066.
46. Yu, A.; Xiao, Y.; Shang, W.; Chen, L.; Shen, H.; Cheng, Q.; Liu, L.; Zhang, L.; Piao, Y.; Sun, Y., Synthesis of a Nanoporous Oxygen-Vacancy-Rich Iron-Nickel Double Hydroxide Composite as a High-Performance Electrocatalyst for Oxygen Evolution Reaction. *J. Electrochem. Soc.* **2022,** *169* (8), 082510.
47. Kirakosyan, A.; Lee, D.; Choi, Y.; Jung, N.; Choi, J., Poly (styrene sulfonic acid)-grafted carbon black synthesized by surface-initiated atom transfer radical polymerization. *Molecules* **2023,** *28* (10), 4168.
48. Zhang, Y.; Liu, W.; Yao, W.; Kang, L.; Gao, E.; Fedin, V. P., An electrochemical sensor based on carbon composites derived from bisbenzimidazole biphenyl coordination polymers for dihydroxybenzene isomers detection. *Microchim. Acta* **2024,** *191* (1), 20.
49. Liao, Y.; Lin, L.; Liu, J.; Zhang, X.; Li, X., Ultrasensitive simultaneous determination of hydroquinone and catechol by Ni3ZnC0. 7/Ni porous composites derived from Ni/Zn-MOF. *J. Electroanal. Chem.* **2024,** *954*, 118028.
50. Chen, J.; Li, S.; Chen, Y.; Yang, J.; Dong, J.; Lu, X., l-cysteine-terminated triangular silver nanoplates/MXene nanosheets are used as electrochemical biosensors for efficiently detecting 5-hydroxytryptamine. *Anal. Chem.* **2021,** *93* (49), 16655-16663.
51. Zhao, G.; Wang, T.; Li, L.; Tang, Y.; Qin, Q.; Wu, C., Heteroatoms doped yolk-shell hierarchically porous carbon derived from ZIF-8 for electrochemical sensing. *Carbon* **2021,** *183*, 291-300.
52. Huang, L.; Cao, Y.; Diao, D., Electrochemical activation of graphene sheets embedded carbon films for high sensitivity simultaneous determination of hydroquinone, catechol and resorcinol. *Sens. Actuators B Chem.* **2020,** *305*, 127495.
53. Ansari, A.; Jacovone, R. M. S.; Nadres, E. T.; Đỗ, M.; Rodrigues, D. F., Optimization of batch and packed-bed column Cr (VI) adsorption of an amine-rich chitosan/polyethyleneimine composite: application in electroplating wastewater treatment. *Environmental Science: Water Research & Technology* **2024,** *10* (7), 1572-1585.
54. Bennett, J. A.; Socash, T.; Khamis, N.; Justik, M. W., Electrochemical investigation of the oxidation of phenolic compounds using hypervalent iodine oxidants. *ACS omega* **2024,** *9* (47), 47361-47367.
55. Pavitt, A. S.; Bylaska, E. J.; Tratnyek, P. G., Oxidation potentials of phenols and anilines: correlation analysis of electrochemical and theoretical values. *Environmental Science: Processes & Impacts* **2017,** *19* (3), 339-349.
56. Markunas, B.; Yim, T.; Snyder, J., pH-Mediated Solution-Phase Proton Transfer Drives Enhanced Electrochemical Hydrogenation of Phenol in Alkaline Electrolyte. *ACS catalysis* **2024,** *14* (22), 16936-16946.
57. Patel, R.; Singh, V. P.; Hoque, A.; K, H.; Gaur, U. K.; Sharma, M., Ultrathin Layered Vanadyl Phosphate Nanosheets as an Ultrasensitive Electrochemical Sensor for

Dihydroxybenzene Isomers in Biological and Environmental Matrices. *ACS Applied Nano Materials* **2025,** *9* (1), 178-189.

58. Koçak, Ç. C., Simultaneous and sensitive determination of hydroquinone, catechol, and resorcinol with a palladium nanoparticles/poly (bromocresol green) modified glassy carbon electrode. *Analytical Methods* **2025,** *17* (27), 5662-5671.

59. Mashhadizadeh, M. H.; Heydarzad, M., Development of novel electrochemical sensor based on Co-Fe layered double hydroxide for simultaneous determination of Hydroquinone, Catechol, and Resorcinol. *Microchemical Journal* **2024,** *206*, 111437.

60. Ahmed, Y. M.; Eldin, M. A.; Galal, A.; Atta, N. F., Electrochemical sensor based on PEDOT/CNTs-graphene oxide for simultaneous determination of hazardous hydroquinone, catechol, and nitrite in real water samples. *Scientific Reports* **2024,** *14* (1), 5654.

61. Ferlazzo, A.; Gulino, A.; Neri, G., Scandia-doped zirconia for the electrochemical detection of hazardous dihydroxybenzene (DHB) isomers in water. *Environmental Science: Advances* **2024,** *3* (10), 1392-1399.

62. Wang, G.; Zhang, S.; Wu, Q.; Zhu, J.; Chen, S.; Lei, Y.; Li, Y.; Yi, H.; Chen, L.; Shi, Z.-Q., Simultaneous detection of acetaminophen, catechol and hydroquinone using a graphene-assisted electrochemical sensor. *RSC advances* **2022,** *12* (37), 23762-23768.

63. Xu, Q.-Q.; Wang, Q.-Q.; Liu, Z.-G.; Guo, Z.; Huang, X.-J., Ultrafine Co3O4 nanoparticle-loaded carbon spheres for the simultaneous ultrasensitive electrochemical determination of hydroquinone and catechol. *ACS Sustain. Chem. Eng.* **2023,** *11* (47), 16764-16773.

64. Kashyap, B.; Kumar, R., A novel multi-set differential pulse voltammetry technique for improving precision in electrochemical sensing. *Biosens. Bioelectron.* **2022,** *216*, 114628.

Data Availability Statement

View Article Online
DOI: 10.1039/D6NR00194G

The data supporting this article have been included as part of the Supplementary Information. **Supplementary information**: Additional experimental details include descriptions of materials and methods used in the study, such as preparation of phosphate buffer solution (PBS) with controlled pH and composition. Electrochemical measurements using CV, DPV, and SWV are described in detail. ML-based analysis of the SPCE data is also presented. Further characterization of the synthesized materials using complementary techniques is included to support the main findings. Additional results on sensor selectivity toward potential interfering species, as well as stability and repeatability evaluated through repeated measurements, are provided. Calibration plots used to determine sensor sensitivity and linear response ranges are also included.